Journal of The
Electrochemical Society



# Numerical Simulation of a Novel $H_2/O_2$ Co-Transport Membrane Reactor for Combined $H_2O/H_2$ Removal and Ethylene Production

To cite this article: Yasser M. M. Shoukry *et al* 2023 *J. Electrochem. Soc.* **170** 103502

*Journal of The Electrochemical Society*, 2023 **170** 103502

# Numerical Simulation of a Novel $H_2/O_2$ Co-Transport Membrane Reactor for Combined $H_2O/H_2$ Removal and Ethylene Production

**Yasser M. M. Shoukry,[1] Kevin Huang,[2,*] and Xinfang Jin[1,*,z]**

[1]*Mechanical Engineering Department, University of Massachusetts, Lowell, Massachusetts 01854, United States of America*
[2]*Mechanical Engineering Department, University of South Carolina, Columbia, South Carolina 29208, United States of America*

To cut $CO_2$ emissions, we propose to directly convert shale gas into value-added products with a new $H_2/O_2$ co-transport membrane (HOTM) reactor. A Multiphysics model has been built to simulate the membrane and the catalytic bed with parameters obtained from experimental validation. The model was used to compare C2 yield and $CH_4$ conversion rate between the membrane reactor and the state-of-the-art fixed-bed reactor with the same dimensions and operating conditions. The results indicate that (1) the membrane reactor is more efficient in consuming $CH_4$ for a given amount of fed $O_2$. (2) The C2 selectivity of the membrane reactor is higher due to the gradual addition of $O_2$ into the reactor. (3) The current proposed membrane reactor can have a decent proton molar flux density but most of the proton molar flux will contribute to producing $H_2O$ on the feed side under the current operating conditions. The paper for the first-time projects the performance of the membrane reactor for combined $H_2O/H_2$ removal and C2 production. It could be used as important guidance for experimentalists to design next generation natural gas conversion reactors.

 [DOI: 10.1149/1945-7111/acfc6b]

Manuscript submitted April 11, 2023; revised manuscript received September 7, 2023. Published October 9, 2023. *This paper is part of the JES Focus Issue on Multiscale Modeling, Simulation and Design: In Honor of Ralph E. White.*

Supplementary material for this article is available online

## List of Symbols

### Common symbols

| | |
|---|---|
| $C_X$ (mol/m$^3$) | Molar concentration of species X |
| $F$ (A.s/mol) | Faraday's constant |
| $N_X$ (mol/m$^2$/s) | Molar flux of species X |
| $R$ (J/mol/K) | universal gas constant |
| $T$ (K) | Temperature |
| [X] | Lattice concentration of species X |

### Symbols for membrane calculations

| | |
|---|---|
| $D_X$ (m$^2$/s) | Diffusivity of species X |
| $D_X^o$ (m$^2$/s) | Pre-exponential factor for diffusivity of species X |
| $E_k$ (kJ/mol) | Activation energy |
| $e'$ | Electron |
| $h^{\cdot}$ | Electron hole |
| $\boldsymbol{J}_X$ (A/m$^2$) | Electric current density carried by species X |
| $K_m$ | Equilibrium constant for reaction m |
| $\Delta H_m$ (kJ/mol) | Enthalpy of reaction m |
| $\Delta S_m$ (J/mol.K) | Entropy of reaction m |
| $V_O^{\cdot\cdot}$ | Oxygen vacancy |
| $Z_X$ | Charge number for species X |
| $\varepsilon_X$ | Volume fraction of phase X |
| $\phi_X$ (V) | Potential of phase X |
| $\sigma_X$ (S/m) | Electrical conductivity of phase X |
| $\tau_X$ | Tortuosity factor of phase X |
| $\mu_X^o$ | Electrochemical potential of species X at standard conditions |

### Symbols for catalytic reactor calculations

| | |
|---|---|
| $r_j$ | Reaction rate of $j$th reaction |
| $K_j$ (mol$^{-1}$ × g$^{-1}$ × s$^{-1}$ × Pa$^{-(m+n)}$) | Pre-exponential factor for $j$th reaction |
| $E_a$ (J/mol) | Activation energy |
| $m_j$, $n_j$ | Reaction order for $j$th reaction |
| $K_{j,i}$ (Pa$^{-1}$) | Adsorption constant for $i$th species in $j$th reaction |
| $\Delta H_{ad,i,j}$ (J/mol) | Adsorption enthalpy for $i$th species in $j$th reaction |
| $R_i$ | Source term for the species i |
| $S_{C_2}$ | C2 products selectivity |
| $u$ (m/s) | Flow velocity inside the reactor |
| $X_{CH4}$ | Percentage of consumed $CH_4$ |
| $Y_{C_2}$ | Yield of C2 products |

Due to the increase in oil price in the last decades, direct natural gas (NG) conversion into high-value petrochemical products, such as $C_2H_4$, has garnered interest.[1] Direct methane conversion (DMC) approaches[2,3] convert $CH_4$ into value-added chemicals in a single step, such as oxidative coupling of methane (OCM),[4,5] oxidative dehydrogenation of ethane (ODHE),[6] and non-oxidative

*Electrochemical Society Member.
[z]E-mail: Xinfang_Jin@uml.edu

dehydrogenation of methane (NODHM).[7,8] The first two methods have been studied thoroughly and implemented in commercial reactors. However, challenges remain to achieve high $CH_4$ conversion at high C2 selectivity.

There are three main categories of reactors reported in open literature. The first one is the fixed-bed reactor,[9] in which reactants are mixed at the inlet and reacting at the surface of catalyst bed. In such a reactor there is very low control on the oxidation process so usually $O_2$ with less than the stoichiometric ratio is fed to avoid the complete oxidation of $CH_4$. Due to this limitation, the C2 yields of this type of reactors can barely exceed 25%.[10] The second category is the moving or fluidized bed reactors,[11] which can achieve C2 yields of 50% but at the cost of constant replenishing of the solid catalyst particles to avoid coke buildup as well as high pumping power consumption to keep the catalyst particles suspended.[12] The third category is membrane reactor,[13] in which $O_2$ is fed gradually along the length of the reactor allowing for easier control on $O_2$ concentration and thus the production of the desired C2 products. The flow of $O_2$ to the reactor is done through a membrane that selectively allows the passage of oxide ions. The performance comparison between these reactors and fixed-bed reactors was reported in various studies.[14–16]

Combining the DMC reaction catalysts with ionic transport membranes opens the door for discovering new multi-purpose reactors. The proposed membrane in this work is a $H^+/O^{2-}$ co-ionic transport membrane composed of $BaZr_{0.8}Y_{0.2}O_{3-\delta}$ (also known as BZY).[17,18] $H_2O$ and $H_2$ are by-products of the DMC reaction, which are removed through the membrane, while oxide ions are transported in the reversed direction to supply $O_2$ for $CH_4$ conversion at the sweep side. There are a few experimental studies in the literature integrating solid oxide electrolysis cells (SOEC) with certain catalyst beds to convert $CH_4$ to higher-value products. SOECs are characterized by their sophisticated multilayer assembly and reliance on an external power supply. Liu et al.[19] integrated SOEC using BZY electrolyte with an Fe-Al/$SiO_2$ catalyst reactor for direct non-oxidative dehydrogenation of $CH_4$ and demonstrated that the in situ removal of $H_2$ gas helped to improve the conversion efficiency of $CH_4$. In addition, Morejudo et al.[20] reported an increase in aromatic yields when using SOEC with BZY electrolyte in a nonoxidative methane dehydroaromatization reactor.

Here, we will investigate integrating a single-layer BZY membrane with a catalyst bed without external power supply. In this study, we will use numerical simulations to determine the performance of the new $H_2/O_2$ co-transport membrane (HOTM) reactor and compare it against the state-of-the-art fixed-bed reactor. It will provide insights into the performance gains in terms of $CH_4$ conversion rate and C2 selectivity by removing $H_2O/H_2$ and adding $O_2$ through the membrane gradually along the reactor flow direction. The model will be validated by experimental data from the lab scale and then used to project performance under different operating temperatures.

## Types of Reactors

In this work, two different types of reactors are simulated. The first type is the membrane reactor previously described in the introduction section, and the second one is a fixed-bed reactor for benchmark comparison and validation. Figure 1 illustrates the working principle of the two reactors. The membrane of the first type is made of the perovskite material BZY ($BaZr_{0.8}Y_{0.2}O_{2.8}$), which will be responsible for co-transporting oxide ions and protons in opposite directions through the wall of the reactor. The charge carrier species in the membrane are shown in Fig. 1.

According to defect chemistry of BZY material,[21,22] oxide ions are transported as oxygen vacancies ($V_O^{\bullet\bullet}$); protons are transported as hydroxide ($OH_O^{\bullet}$). Electron holes ($h^{\bullet}$) also exist to compensate for the charge neutrality of the membrane. The inner side of the reactor (sweep side) in both reactors is filled with $La_2O_3$-CaO-modified $CeO_2$ catalyst with a 34% porosity. The inlet gas composition in the membrane reactor is almost 100% $CH_4$ while $O_2$ is gradually added along the reactor wall; on the other hand, $H_2O$ and $H_2$ are transported to the feed side through the membrane. The total amount of oxide ions passing through the membrane and contributing to $O_2$ flux on the reactor side is calculated in each operating temperature and will be used to determine the gas composition at the inlet of the fixed-bed reactor. A 10-step reactions model[23] is used to simulate the catalytic reactions of the catalyst bed in the sweep (reactor) side. The 10-step reactions model is depicted in Fig. 1, with blue arrows indicating a catalytic reaction while the red arrow indicating a gas phase reaction. The details of the reaction rate calculations and kinetic parameters can be found in Tables I and II respectively.

Figure 2 shows the computational domains used for each reactor. For the Membrane reactor, there are two domains, which are co-axially symmetric. One domain (depicted in light blue) representing the inner part filled with the catalyst, and the other thin domain (depicted in light red) representing the membrane. The fixed-bed reactor has only one computational domain (also axisymmetric). The inner catalytic part (sweep side) has a radius of 10 mm, the membrane thickness is 0.2 mm, and the reactor total length is 400 mm. The reactants (for both sweep and feed sides) enter the reactor from the bottom of the domain and exit from the upper boundary.

## Mathematical Models

This section describes the mathematical model used to simulate the two types of reactors shown in the previous section. Starting with the catalyst bed reactor, which is modeled as a plug flow passing through $La_2O_3$/CaO catalyst. The species transport is calculated based on the following equation:

$$-\nabla D_i \nabla C_i + u.\nabla C_i = R_i \quad [1]$$

The kinetic model is based on the work done by Stansch et al.,[23] where the Oxidative Coupling of Methane is broken down into 10 steps as shown in Table I. These steps include thermal cracking, steam reforming and water gas shift reactions. The reaction rates for reaction 1 to 6 are Hougen-Watson type rate equations, while the rest are power-law rate equations. All the reactions are associated with catalytic rates except for reaction 7 which is a gas phase reaction. The calculated reaction rates are used to calculate the source term in Eq. 1.

The values of the kinetic parameters are based on data from Stansch et al.,[23] in which the results from a series of experiments covering a wide range of conditions ($1 < pO_2 < 20$ kPa, $10 < pCH_4 < 95$ kPa, $700 < T < 955$ °C) were used to determine the parameters, which are shown in Table II. Moreover, in this work, the full model is validated against the experimental data reported by Ching et al.[24] The results of the validation are presented in the next section.

The evaluation of the reactor's performance is done using two metrics, the first one is $CH_4$ conversion rate ($X_{CH_4}$), and the second metric is the C2 yield ($Y_{C_2}$). Those two metrics are correlated by the selectivity of C2 ($S_{C_2}$). The following equations show the definition of these metrics:

$$Y_{C_2} = S_{C_2} \bullet X_{CH4} \quad [2]$$

$$S_{C_2} = \frac{[2 \times (N_{C_2H_4,out} - N_{C_2H_4,in}) + 2 \times (N_{C_2H_6,out} - N_{C_2H_6,in})]}{N_{CH4,in} - N_{CH4,out}} \quad [3]$$

$$X_{CH4} = \frac{N_{CH4,in} - N_{CH4,out}}{N_{CH4,in}} \quad [4]$$

The second part of the mathematical model is for the membrane. As mentioned above, the proposed membrane is composed of

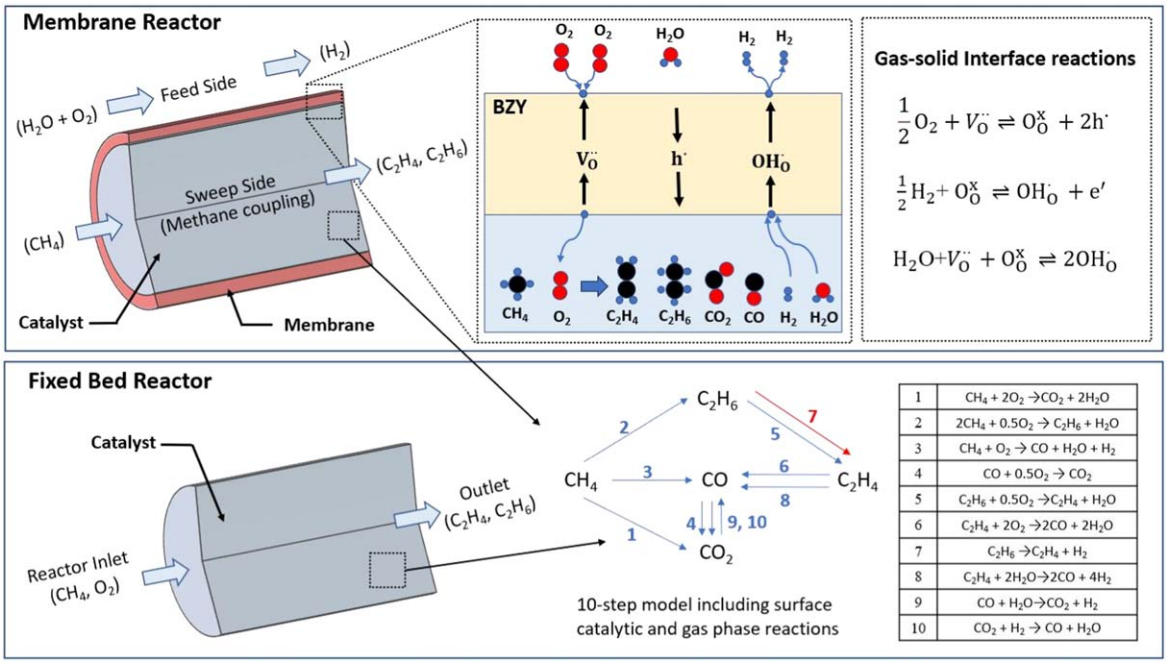


**Figure 1.** Illustration of the two types of reactors to be studied in this work.

**Table I. Reaction steps for the kinetic model.**

| Index | Reaction | Reaction Kinetics |
|---|---|---|
| 1 | $CH_4 + 2O_2 \rightarrow CO_2 + 2H_2O$ | $r_1 = \frac{(k_{01} \cdot e^{-\frac{E_a}{RT}}) \cdot P_{CH_4}^{m_1} \cdot P_{O_2}^{n_1}}{\left(1 + K_{1,CO_2} \cdot e^{-\frac{\Delta H_{ad,CO_2,1}}{RT}} \cdot P_{CO_2}\right)^2}$ |
| 2 | $2CH_4 + 0.5O_2 \rightarrow C_2H_6 + H_2O$ | $r_2 = \frac{k_{02} \cdot e^{-\frac{E_a}{RT}} \cdot \left(K_{0O_2} \cdot e^{-\frac{\Delta H_{adO_2}}{RT}} P_{O_2}\right)^{n_2} P_{CH_4}}{\left[1 + (K_{0,O_2} \cdot e^{-\frac{\Delta H_{ad,O_2}}{RT}} \cdot P_{O_2})^n + K_{2,CO_2} \cdot e^{-\frac{\Delta H_{ad,O_2}}{RT}} P_{O_2}\right]^2}$ |
| 3 | $CH_4 + O_2 \rightarrow CO + H_2O + H_2$ | $r_3 = \frac{(k_{03} \cdot e^{-\frac{E_a}{RT}}) \cdot P_{CH_4}^{m_3} \cdot P_{O_2}^{n_3}}{\left(1 + K_{3,CO_2} \cdot e^{-\frac{\Delta H_{ad,CO_2,3}}{RT}} \cdot P_{CO_2}\right)^2}$ |
| 4 | $CO + 0.5O_2 \rightarrow CO_2$ | $r_4 = \frac{(k_{04} \cdot e^{-\frac{E_a}{RT}}) \cdot P_{CO}^{m_4} \cdot P_{O_2}^{n_4}}{\left(1 + K_{4,CO_2} \cdot e^{-\frac{\Delta H_{ad,CO_2,4}}{RT}} \cdot P_{CO_2}\right)^2}$ |
| 5 | $C_2H_6 + 0.5O_2 \rightarrow C_2H_4 + H_2O$ | $r_5 = \frac{(k_{05} \cdot e^{-\frac{E_a}{RT}}) \cdot P_{C_2H_6}^{m_5} \cdot P_{O_2}^{n_5}}{\left(1 + K_{5,CO_2} \cdot e^{-\frac{\Delta H_{ad,CO_2,5}}{RT}} \cdot P_{CO_2}\right)^2}$ |
| 6 | $C_2H_4 + 2O_2 \rightarrow 2CO + 2H_2O$ | $r_6 = \frac{(k_{06} \cdot e^{-\frac{E_a}{RT}}) \cdot P_{C_2H_4}^{m_6} \cdot P_{O_2}^{n_6}}{\left(1 + K_{6,CO_2} \cdot e^{-\frac{\Delta H_{ad,CO_2,6}}{RT}} \cdot P_{CO_2}\right)^2}$ |
| 7 | $C_2H_6 \rightarrow C_2H_4 + H_2$ | $r_7 = k_{07} \cdot e^{-\frac{E_{a7}}{RT}} P_{C_2H_6}$ |
| 8 | $C_2H_4 + 2H_2O \rightarrow 2CO + 4H_2$ | $r_8 = k_{08} \cdot e^{-\frac{E_{a8}}{RT}} P_{C_2H_4}^{m_8} \cdot P_{H_2O}^{n_8}$ |
| 9 | $CO + H_2O \rightarrow CO_2 + H_2$ | $r_9 = k_{09} \cdot e^{-\frac{E_{a9}}{RT}} P_{CO}^{m_9} P_{H_2O}^{n_9}$ |
| 10 | $CO_2 + H_2 \rightarrow CO + H_2O$ | $r_{10} = k_{10} \cdot e^{-\frac{E_{a10}}{RT}} P_{CO_2}^{m_{10}} P_{H_2}^{n_{10}}$ |

perovskite material BZY. Figure 1 shows the charge carriers that are responsible for the ionic transport.

Table III lists the reactions occurring at the BZY-gas interface (except reaction 11, which is the overall gas phase reaction, and reaction 15, which is the intrinsic electron hole defect reaction). In addition, the charge carrier diffusivities are listed in Table IV. The validation of these parameters (Tables III and IV) will be discussed in detail in the next section.

**Table II. Kinetic parameters.**

| Index | $k_{0j}$ $mol^{-1} \times g^{-1} \times s^{-1} \times Pa^{-(m+n)}$ | $E_{a,j}$ | $K_{j,CO2}$ | $\Delta H_{ad,CO2}$,kJ/mol | $K_{O2}$,$Pa^{-1}$ | $\Delta H_{ad,O2}$ | $m_j$ | $n_j$ |
|---|---|---|---|---|---|---|---|---|
| 1 | $0.2 \times 10^{-5}$ | 48 | $0.25 \times 10^{-12}$ | −175 | —— | —— | 0.24 | 0.76 |
| 2 | 23.2 | 182 | $0.83 \times 10^{-13}$ | −186 | $0.23 \times 10^{-11}$ | −124 | 1 | 0.4 |
| 3 | $0.52 \times 10^{-6}$ | 68 | $0.36 \times 10^{-13}$ | −187 | —— | —— | 0.57 | 0.85 |
| 4 | $0.11 \times 10^{-3}$ | 104 | $0.4 \times 10^{-12}$ | −168 | —— | —— | 1 | 0.55 |
| 5 | 0.17 | 157 | $0.45 \times 10^{-12}$ | −166 | —— | —— | 0.95 | 0.37 |
| 6 | 0.06 | 166 | $0.16 \times 10^{-12}$ | −211 | —— | —— | 1 | 0.96 |
| 7 | $1.2 \times 10^{7}$ | 226 | —— | —— | —— | —— | —— | —— |
| 8 | $9.3 \times 10^{3}$ | 300 | —— | —— | —— | —— | 0.97 | 0 |
| 9 | $0.19 \times 10^{-3}$ | 173 | —— | —— | —— | —— | 1.0 | 1.0 |
| 10 | $0.26 \times 10^{-1}$ | 220 | —— | —— | —— | —— | 1.0 | 1.0 |

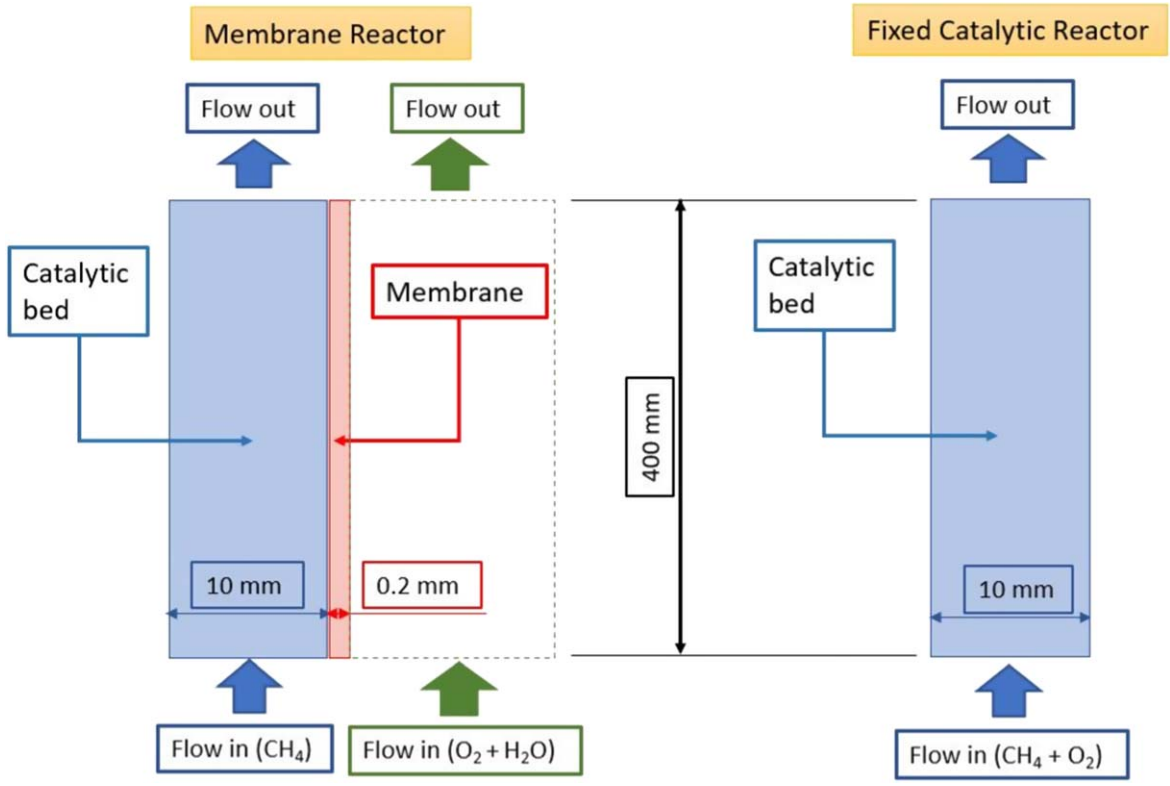


**Figure 2.** Schematic of the computational domains used for the two types of reactors.

**Table III. Equilibrium parameters for BZY-gas interface reactions.**

| Index | Reaction | $\Delta H^o$(kJ/mol) | $\Delta S^o$(J/molK) |
|---|---|---|---|
| 11 | $H_2O \rightleftharpoons H_2 + \frac{1}{2}O_2$ | 245.45 | 52.51 |
| 12 | $\frac{1}{2}O_2 + V^{\cdot\cdot}_{O(BZY)} \rightleftharpoons O^x_{O(BZY)} + 2h^{\bullet}_{(BZY)}$ | −124* | −130* |
| 13 | $\frac{1}{2}H_2 + O^x_{O(BZY)} \rightleftharpoons OH^{\cdot}_{O(BZY)} + e'_{(BZY)}$ | 142.73* | −12.85* |
| 14 | $H_2O + V^{\cdot\cdot}_{O(BZY)} + O^x_{O(BZY)} \rightleftharpoons 2OH^{\cdot}_{O(BZY)}$ | −93.3* | −103.2* |
| 15 | $e' + h^{\bullet} \rightleftharpoons$ null | 250* | 0 |

The equilibrium constant of each reaction can be calculated using the following equation:

$$K_r = e^{\frac{-(\Delta H_r - T\Delta S_r)}{RT}} \quad [5]$$

Where $K_r$ is the equilibrium constant of reaction r, $\Delta H_r$ is the reaction's enthalpy, and $\Delta S_r$ is the reaction's entropy.

The diffusivity ($D_k$) for each charged species is calculated using the following relation:

$$D_k = D_k^o \exp\left(\frac{-E_k}{RT}\right) \quad [6]$$

**Table IV. Transport properties of charge carriers in BZY.**

| Charge carrier | $D_k^o$ (m²/s) | $E_k$ (kJ/mol) | $D_k$ (m²/s) (923 K) This paper | Kee 2013 $D_k$ (m²/s) (923 K) |
|---|---|---|---|---|
| $OH_O^{\cdot}$ | $1.1 \times 10^{-7}$* | 47.3* | $2.31 \times 10^{-10}$ | $5.72 \times 10^{-11}$ |
| $V_O^{\cdot\cdot}$ | $4.5 \times 10^{-7}$* | 90.0* | $3.62 \times 10^{-12}$ | $2.08 \times 10^{-13}$ |
| $h^{\bullet}$ | $2.0 \times 10^{-4}$* | 97.0 | $6.47 \times 10^{-10}$ | $3.41 \times 10^{-12}$ |
| $e'$ | $1.70 \times 10^{-7}$ | 90.0 | $1.37 \times 10^{-12}$ | $1.37 \times 10^{-12}$ |

The conductivity for each charge carrier can then be calculated as:

$$\sigma_k = \frac{D_k \quad Z_k{}^2 F^2}{RT} C_k \qquad [7]$$

Where $\sigma_k$ is the conductivity of the charge carrier $k$, $Z_k$ is the charge number, $F$ is Faraday's constant, $C_k$ is the concentration of species $k$, $R$ is the gas constant, and $T$ is the temperature.

With the Kröger-Vink notation, in the BZY material, there are three positive charged species, including proton $[OH_O^{\cdot}]$, oxygen vacancy $[V_O^{\cdot\cdot}]$ and electron hole $[h^{\bullet}]$, and two negative charged species, which are the acceptor dopant $[Y'_{Zr}]$ and electron $[e']$. To calculate the concentrations of the charge carriers in BZY, the equilibrium equations for reactions 12 and 14 are used:

$$K_{O_2} = \frac{[h^{\bullet}]^2 [O_O^x]}{p(O_2)^{1/2} [V_O^{\cdot\cdot}]} \qquad [8]$$

$$K_{H_2O} = \frac{[(OH)_O^{\cdot}]^2}{p(H_2O)[O_O^x][V_O^{\cdot\cdot}]} \qquad [9]$$

In addition, the charge neutrality equation in BZY can be written as follows:

$$[e'] + [Y'_{Zr}] = 2[V_{O_o}^{\cdot\cdot}] + [h^{\cdot}] + [OH_O^{\cdot}] \qquad [10]$$

Since the lattice oxygen sites are limited to 3, the following equation can be written:

$$[V_O^{\cdot\cdot}] + [O_O^x] + [OH_O^{\cdot}] = 3 \qquad [11]$$

And finally, the intrinsic electron hole defect equilibrium:

$$[h^{\bullet}][e'] = K_I \qquad [12]$$

The number of unknowns in the previous set of equations is 5 ($[V_O^{\cdot\cdot}]$, $[e']$, $[h^{\bullet}]$, $[O_O^x]$, $[OH_O^{\cdot}]$). The five Eqs. 8 to 12 are input in the COMSOL 6.0 model through the Boundary ODEs and DAEs interface and are solved using the Newton non-linear iterative method. It is worth mentioning that two partial pressures of the three gas species should be known ($H_2O$ vapor, $O_2$, and $H_2$), then the third one can be calculated using the gas phase equilibrium equation:

$$K_{gas} = \frac{p(H_2)p(O_2)^{1/2}}{p(H_2O)} \qquad [13]$$

Nernst-Plank equations are used to calculate the potential and the concentration distribution of the charge carriers. Table V summarizes the equations used as well as the previously discussed boundary conditions.

For calculating the gas molar fluxes from and into the membrane, the equations proposed by Kee[22] were used and are listed below:

$$N_{H_2O} = -N_{V_O^{\cdot\cdot}} - \frac{1}{2} N_h \frac{p_{O_2}^{1/2}}{p_{O_2}^{1/2} + p_{H_2}} \qquad [14]$$

$$N_{O_2} = \frac{1}{4} N_h \frac{p_{O_2}^{1/2}}{p_{O_2}^{1/2} + p_{H_2}} \qquad [15]$$

$$N_{H_2} = -\frac{1}{2} N_h \frac{p_{H_2}}{p_{O_2}^{1/2} + p_{H_2}} \qquad [16]$$

Where $N_X$ is the molar flux density of the gas species or ionic species X, and the molar flux inside the membrane is related to the current density through the following relation:

$$N_X = \frac{\boldsymbol{J}_X}{Z_X \quad F} \qquad [17]$$

It is worth noting that according to Eqs. 14, 15, and 16, the gas molar fluxes are dependent on the gas composition, which means for the same molar flux of charge carriers, the gas flux of $O_2$ for example will differ from one side of the membrane to the other side.

## Experimental Validation

The validation is split into two main parts, the first part is to validate the mathematical model of the membrane. The second part is to validate the mathematical model of the catalyst bed (inner or sweep side).

***Validation of the BZY membrane.***—Using various sources,[21,25–27] Kee[22] calculated the equilibrium constants of reactions 11 to 15. We attempted to use these values to predict the mol percentage of $OH_O^{\cdot}$ in BZY at an $H_2O$ partial pressure of 23 hPa and compare with the experimentally measured data by Kreuer.[21] A discrepancy under all temperatures has been observed, as shown in Fig. 3a. According to Nernst-Einstein's equation (Eq. 7), conductivity $\sigma_k$ is the product of concentration $C_k$ and diffusivity $D_k$ of species k. As a result, thermodynamic properties (concentration of species) and transport properties (diffusivity of species) are highly correlated, and accurate prediction of the concentration is essential. To calculate those two sets of properties inversely, experimental data of both conductivity and concentration of charged species are necessary. Therefore, in this paper, we take a two-step approach to get those two sets of properties.

Firstly, we inversely calculated the thermodynamic properties of the related reactions shown in Table III. Among these reactions, reaction 11 is the gas phase water formation, in which the enthalpies, and entropies of formation for $O_2$, $H_2$ and $H_2O$ are well known and established, therefore, this reaction's parameters are given. Besides, the reactions in Table III are not fully independent. This can be seen by subtracting reactions 11, 12, and 15 from reaction 14, which results in reaction 13. As a result, we dropped reaction 13 and only enthalpies and entropies of reactions 12, 14 and 15 were optimized to fit the experimental data for $OH_O^{\cdot}$ ion concertation reported by Kreuer.[21] A comparison between the model prediction with optimized parameters and the experimental data is shown in Fig. 3a. The optimized parameters are given in Table III. The parameters that are denoted with asterisks are the ones different from those reported by Kee.[22]

**Table V. Transport equations for the membrane.**

| Species | Equation used | BC (r = 0) | BC (r = L) |
|---|---|---|---|
| $C_{V_O^{\cdot\cdot}}$ | $\nabla \boldsymbol{J}_{V_O^{\cdot\cdot}} = -Z_{V_O^{\cdot\cdot}} F D_{V_O^{\cdot\cdot}} \nabla^2(C_{V_O^{\cdot\cdot}}) - \frac{D_{V_O^{\cdot\cdot}} F^2 Z_{V_O^{\cdot\cdot}}{}^2}{RT} C_{V_O^{\cdot\cdot}} \nabla^2(\phi)$ | $(C_{V_O^{\cdot\cdot}})_0$ | $(C_{V_O^{\cdot\cdot}})_L$ |
| $C_{OH_O^{\cdot}}$ | $\nabla \boldsymbol{J}_{OH_O^{\cdot}} = -Z_{OH_O^{\cdot}} F D_{OH_O^{\cdot}} \nabla^2(C_{OH_O^{\cdot}}) - \frac{D_{OH_O^{\cdot}} F^2 Z_{OH_O^{\cdot}}{}^2}{RT} C_{OH_O^{\cdot}} \nabla^2(\phi)$ | $(C_{OH_O^{\cdot}})_0$ | $(C_{OH_O^{\cdot}})_L$ |
| $\phi_{BZY}$ | $\nabla \boldsymbol{J}_{O_O^{\times}} = -Z_{h^{\cdot}} F D_{h^{\cdot}} \nabla^2(C_{h^{\cdot}}) - \frac{D_{h^{\cdot}} F^2 Z_{h^{\cdot}}{}^2}{RT} C_{h_O^{\cdot}} \nabla^2(\phi)$ | $\phi_{BZY0} = 0$ | $J_{V_O^{\cdot\cdot}} + J_{OH_O^{\cdot}} + J_{h^{\cdot}} = 0$ |
| $C_{O_O^{\times}}$ | $C_{h^{\cdot}} + C_{OH_O^{\cdot}} + 2C_{V_O^{\cdot\cdot}} - C_{Y'_{Zr}} = 0$ | — | — |

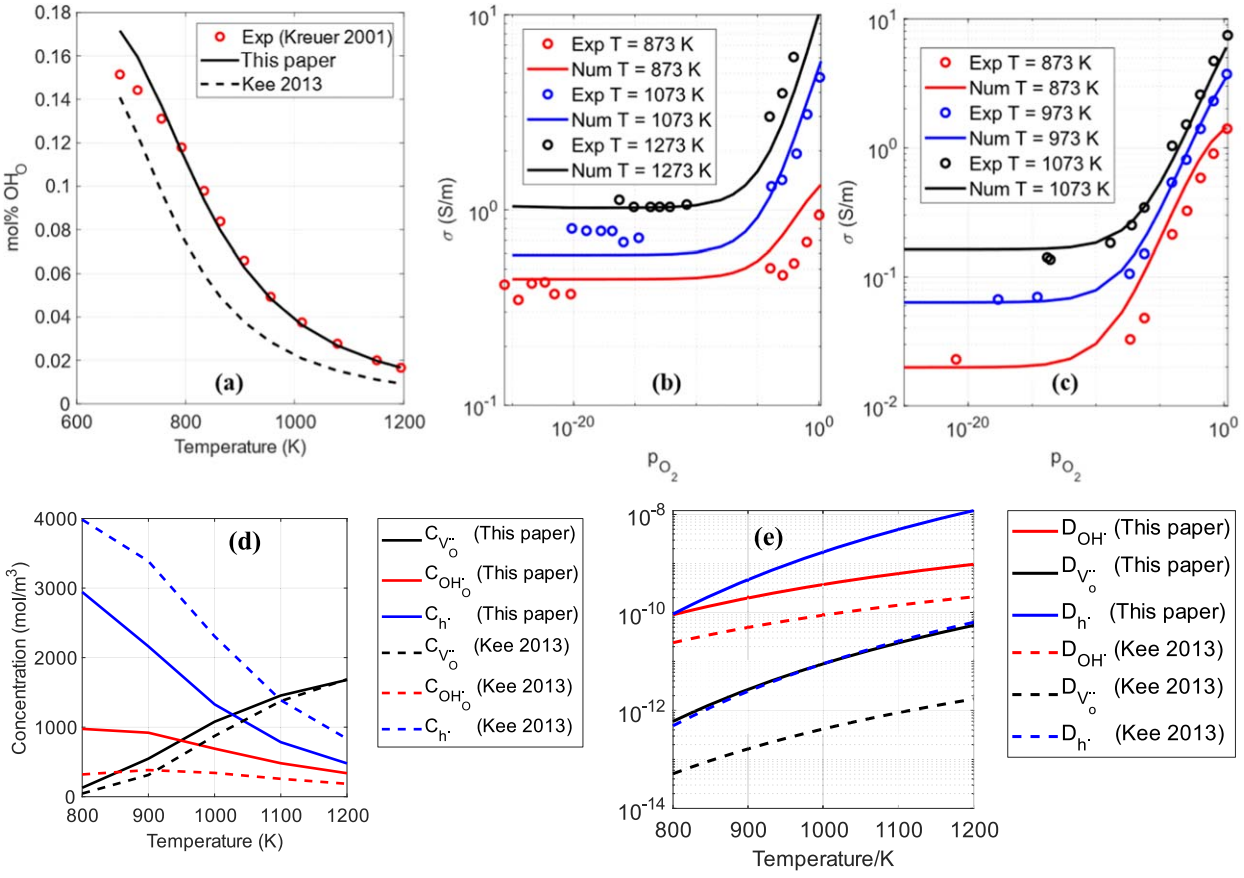


**Figure 3.** (a) Hydroxide mol fraction in BZY (b) Overall BZY conductivity in dry conditions (c) Overall BZY conductivity in wet conditions (d) Molar concentration at $p$H2O = 0.023 & $p$O2 = 0.2 (e) Diffusivity of charge carriers.

Secondly, we calculated the pre-exponential factor and the activation energies used to evaluate diffusivities of charge carriers in BZY, which are shown in Table IV with the values denoted with asterisks for the ones which are different from those in Kee's paper.[22] The experimental conductivity data provided by Nomura[17] was used to inversely calculate those parameters. Comparisons between the model predictions and experimental conductivities in both dry and wet conditions are shown in Figs. 3b and 3c.

For step 2, with the conductivity under dry conditions, the dominant reaction is Reaction 12 from Table III with vacancies and electron holes as the charge carriers. Under high $O_2$ partial pressure range, more Oxygen atoms will be inserted into the lattice producing more electron holes with a higher diffusivity. Therefore, the diffusivity of holes is most sensitive to the inclined part of Fig. 3b, while the diffusivity of vacancies is directly related to the horizontal part where holes are absent. Under the wet conditions (Fig. 3c), $OH_O^{\cdot}$ ion is the dominant charged species, especially in the low $O_2$ partial pressure range. So, $OH_O^{\cdot}$ diffusivity is strongly correlated with the horizontal part of the wet conductivity data. And finally, BZY is known to be dominated by electron holes with negligible electron concentration, so the parameters for electrons were not adjusted.

To further understand the differences between our optimized parameters and those calculated by Kee,[22] the molar concentrations of the charge carriers were plotted against the temperature with $p_{H_2O} = 0.023$ & $p_{O_2} = 0.2$, as shown in Fig. 3d, Kee's parameters seem to underestimate the water vapor uptake (reaction 14), and thus predicts lower $OH_O^{\cdot}$ molar concentration. As a result, the available vacancies are consumed by the oxidation reaction (reaction 12) resulting in higher electron hole concentration. A comparison between the diffusivities is also shown in Fig. 3e, Kee's parameters[22] predict that the diffusivity of the $OH_O^{\cdot}$ ion is higher than that of the electron hole, which is very hard to achieve considering the much smaller size of electrons. In addition, when calculating the overall conductivity using Kee's parameters,[22] the lower electron hole concentration is compensated by its higher predicted concentration. Based on the supplemental section, we also

find that with Kee's parameters, the predicted open circuit voltage of BZY electrolyte will be higher than its Nernst Potential, which is contradicted with what reported in the experiment.[28] The prediction of this paper agrees with the experimental open circuit voltage perfectly by confirming that the diffusivity of electron holes is higher than that of the protons.

***Validation of the DMC catalyst bed.—***The second part is to validate the mathematical model of the catalyst bed (inner or sweep side). COMSOL 6.0 was used to create a 2D domain with the same dimensions mentioned by Ref. 24. Equation 1 is used to model the species transport in the reactor, and the kinetic parameters were based on the data reported by Stansch.[23] The simulations were done using the same boundary conditions as mentioned in Ref. 24. Figure 4 compared the C2 yields and the $CH_4$ conversion rates from the numerical solution in this work (represented in solid blue lines) with both the experimental and numerical (represented in red and black circles respectively) results in Ref. 24. The current numerical solution shows good agreement with the experimental results. In addition, the deviation from the experimental results is smaller than that of the numerical solution reported in the original reference.

## Simulation Results

COMSOL 6.0 was used to create the numerical models for both the membrane reactor and fixed-bed reactor with the 2D domains described in the section "Types of Reactors" and governing equations described in the section "Mathematical models." The details of the reactor dimensions, species diffusivities, flow velocity and the boundary conditions can be found in Table VI.

Two reactors were simulated at 4 different temperatures ranging from 923 K up to 1073 K. The runs started with the membrane reactor to determine the amount of $O_2$ that will be supplied to the sweep side and compare it to the total flow going into the reactor. The change in temperature caused the differences in reaction rates and thus led to different internal gas composition in each case. The different gas composition affected the amount of $O_2$ that will be supplied to the sweep side in the membrane reactor for each temperature. Figure 5a shows $O_2$ molar flux as a percentage of the total gas flow going into the reactor. The amount of oxide ions going through increases with temperature up to 1023 K then it drops when the temperature further increases to 1073 K. The fixed bed reactor was simulated with the same $O_2$ percentage as that of the membrane reactor. C2 yields and $CH_4$ conversion rates in both reactors are compared under different temperatures.

Figure 5b shows a comparison between the two reactors at different temperatures. It shows that the membrane reactor is superior to the fixed bed reactor in $CH_4$ conversion rate (20% to 60% higher). In addition, the membrane reactor is more efficient in producing C2 products as shown in Figs. 5c and 5d. The C2 Selectivity of the membrane reactor is almost 100% at lower temperatures, and the C2 yields are better in the membrane reactor (48% to 82% higher) over the full range of temperatures.

Examining the species molar concentration plots in Fig. 6 can give a clearer picture on what is happening in the two reactors. The molar concentration of $C_2H_4$ in the membrane reactor is double that of $C_2H_6$. In addition, it is higher compared to that of the Fixed-bed

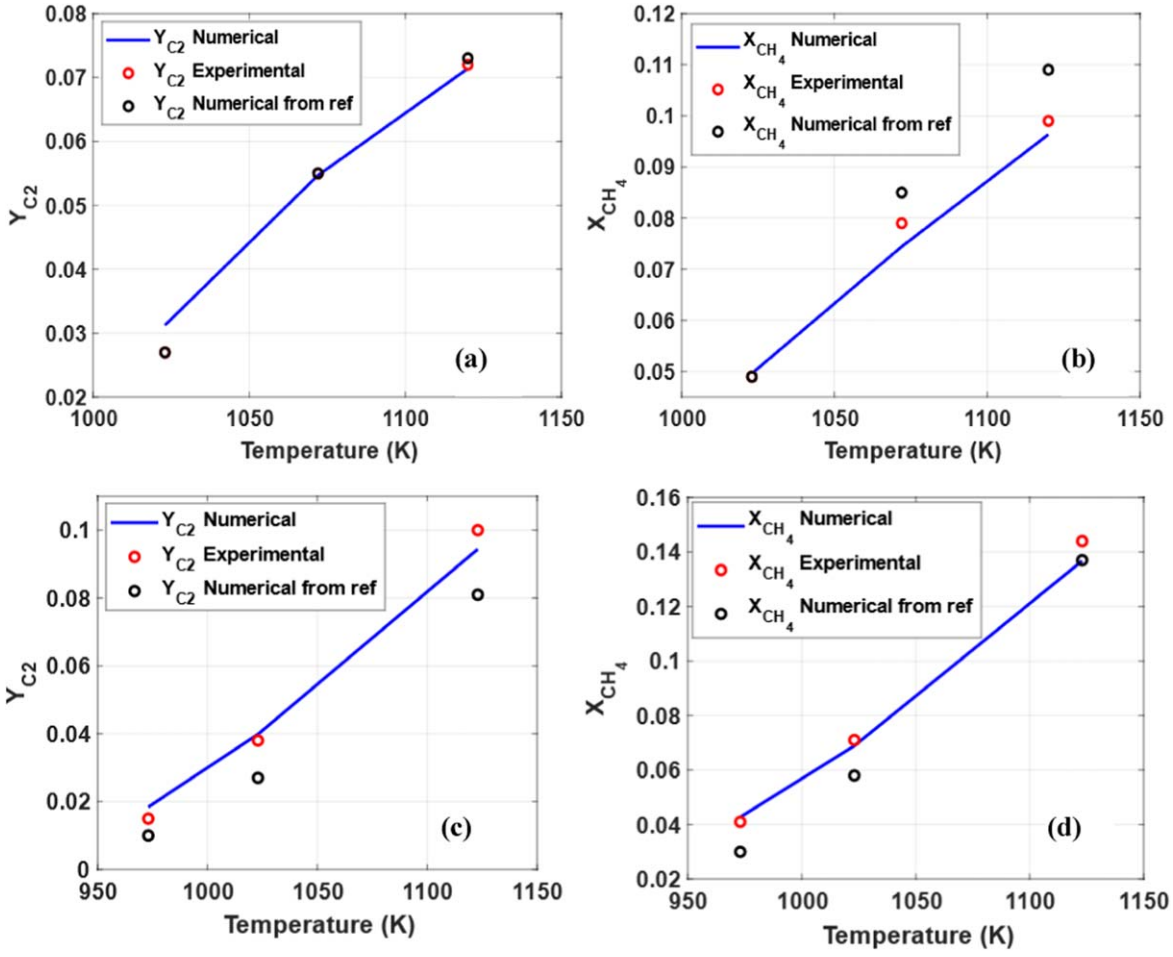


**Figure 4.** Experimental data vs numerical solution, (a) and (b) fixed-bed reactor yields at low $O_2$ concentration; (c) and (d) fixed-bed reactor yields at high $O_2$ concentration.

**Table VI. Simulation parameters.**

| Parameter | Value | References |
|---|---|---|
| **Common Parameters for Both Reactors** | | |
| Reactor length | 400 [mm] | —— |
| Reactor diameter | 20 [mm] | |
| Operating temperature | 923–1073 [K] | |
| $CH_4$ stream velocity | 0.05 [m $s^{-1}$] | |
| $CO_2$ diffusivity | $1.39 \times 10^{-4}$ [$m^2$ $s^{-1}$] | 32 |
| CO diffusivity | $1.45 \times 10^{-4}$ [$m^2$ $s^{-1}$] | |
| $O_2$ diffusivity | $1.52 \times 10^{-4}$ [$m^2$ $s^{-1}$] | |
| $CH_4$ diffusivity | $1.57 \times 10^{-4}$ [$m^2$ $s^{-1}$] | |
| $C_2H_6$ diffusivity | $1.31 \times 10^{-4}$ [$m^2$ $s^{-1}$] | |
| $C_2H_4$ diffusivity | $1.37 \times 10^{-4}$ [$m^2$ $s^{-1}$] | |
| $H_2O$ diffusivity | $1.95 \times 10^{-4}$ [$m^2$ $s^{-1}$] | |
| $H_2$ diffusivity | $6.20 \times 10^{-4}$ [$m^2$ $s^{-1}$] | |
| **Membrane Reactor Specific Parameters** | | |
| Membrane thickness | 0.2 [mm] | —— |
| Feed gas composition | 20% $O_2$ | —— |
| Sweep gas composition | 99.9% $CH_4$ | —— |
| **Fixed-Bed Reactor Specific Parameters** | | |
| Inlet gas composition | Variable depending on temperature (See Fig. 5a) | —— |

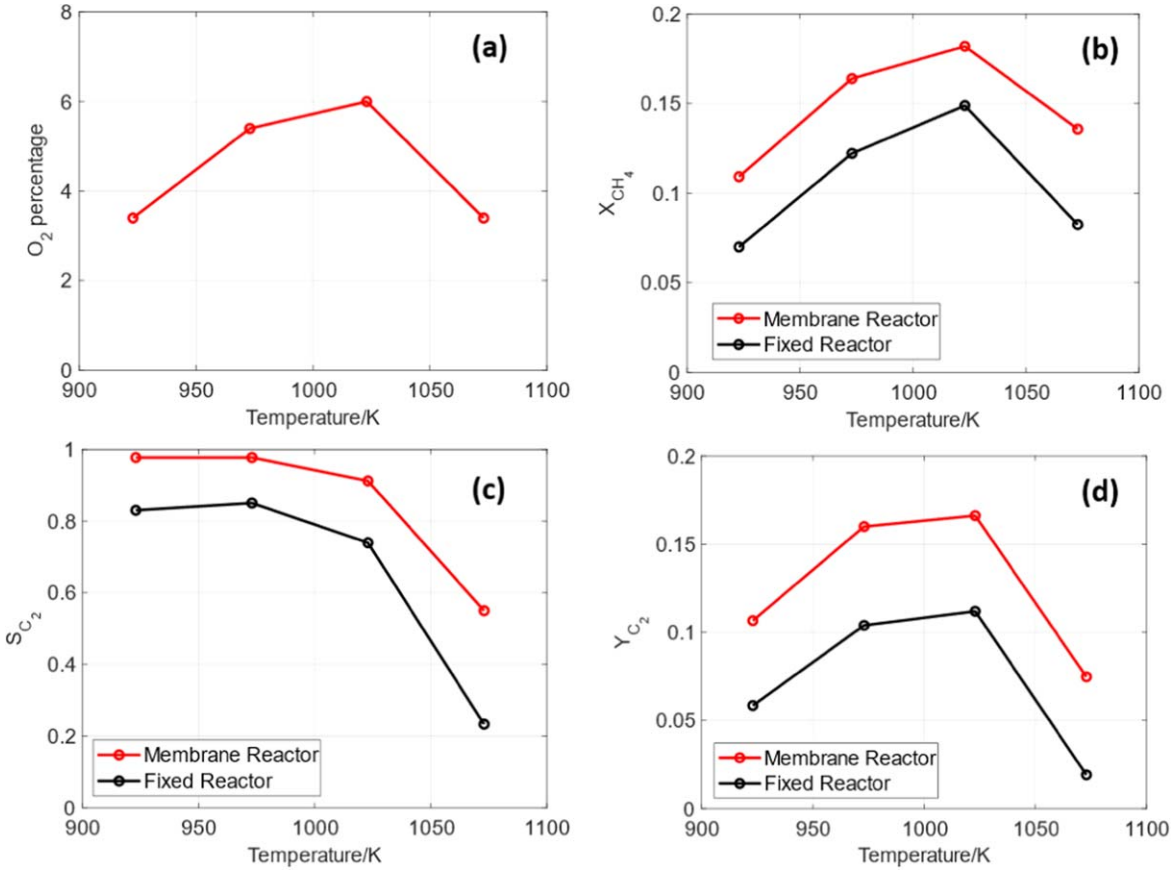


**Figure 5.** (a) $O_2$ flow as a percentage of total gas flow in the membrane reactor; Comparison between fixed-bed reactor and the membrane reactor: (b) CH4 conversion rate (c) C2 products selectivity (d) C2 Yield.

reactor. Another observation is the concentration of $H_2O$ and $H_2$ in both reactors. The average concentration is smaller in the membrane reactor, due to the proton transfer to the feed side through the membrane and the absence of a similar mechanism in the fixed-bed reactor. Finally, the production of $CO_2$ and CO is lower in the membrane reactor.

Despite feeding both reactors with the same molar fraction of $O_2$, there is a big difference in the percentage of consumed $CH_4$ as seen in Fig. 5b. This can be explained by looking at the reactions of the kinetic model and examining how the rates of the reactions that consume $CH_4$ change with the conditions of each reactor. Reactions 1 and 3 are combustion of methane, which fully (reaction 1) or partially (reaction 3) oxidizes $CH_4$ to become $CO_2$ or CO and $H_2O$.

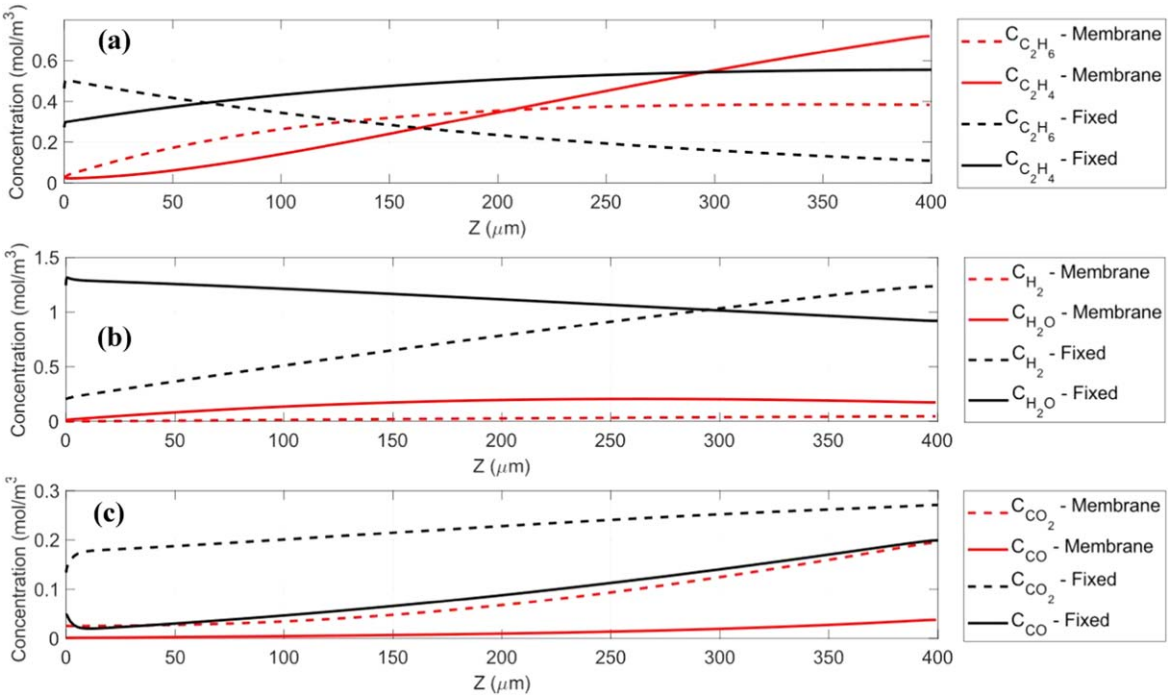


**Figure 6.** Different Species' mole fractions at 1023 K (a) $C_2H_4$ and $C_2H_6$; (b) $H_2$ and $H_2O$; (c) $CO_2$ and CO.

Reaction 2 on the contrary produces $C_2H_6$ and is denoted as oxidative coupling of methane (OCM) reaction.

OCM reaction (reaction 2) is the most efficient in consuming $CH_4$ because it uses half a mole of $O_2$ to react with two moles of $CH_4$, while the combustion reactions (1 and 3) are less efficient, as they respectively use 2 and 1 moles of $O_2$ to oxidize only one mole of $CH_4$.

To get the full picture of what is happening in each reactor, the reaction rates are integrated over the computational domain for both reactors to get that reaction's contribution ($RC_n$) to the overall consumption of $CH_4$ according to the following equation:

$$RC_n = \int r_n.a_n.\rho_c \quad dV \qquad [18]$$

Where $r_n$ is the reaction rate, $a_n$ is the $CH_4$ stoichiometric coefficient of $n$th reaction, and $\rho_c$ is the catalyst density in the bed.

The contribution from each reaction is then divided by the summation of $CH_4$ consumption across all three reactions (1 to 3) to get the normalized percentage contribution ($\%r_n$) of each reaction as shown in the following equation:

$$\%r_n = \frac{RC_n}{\sum_{i=1\to 3} RC_i} \times 100 \qquad [19]$$

The percentages of each reaction contribution are shown in Fig. 7, which shows that the contribution from the combustion reactions (reactions 1 and 3) are much larger in case of the fixed bed reactor across the board, while in the membrane reactor, the OCM reaction (reaction 2) is more dominant, which confirms that the membrane reactor is more efficient in consuming $CH_4$ by producing more C2 products.

Another main difference between those two reactors is that in the membrane reactor, $O_2$ is fed gradually through the membrane wall and is consumed quickly resulting in a lower $O_2$ concentration in the reaction zone, while in the fixed-bed reactor, the full amount of $O_2$ is fed at the inlet, resulting in a higher overall $O_2$ concentration in the reaction zone. This can be seen in Fig. 8, where the maximum $O_2$ concentration of the fixed-bed reactor is two orders of magnitude higher than that of the membrane reactor. To understand how this would affect the reactor performance, $CH_4$ consuming reaction rates (reaction 1 to 3) are calculated at different $O_2$ partial pressures, with other parameters set to constant values ($p_{CH_4} = 95000Pa$, $p_{CO_2} = 1000Pa$). As shown in Fig. 9, Combustion reactions (reactions 1 and 3) scale differently with $O_2$ concentration compared to the efficient OCM reaction (reaction 2). At the lower $O_2$ concentration, the difference is two to three orders of magnitude between reaction 2 and reactions 1 or 3; when the $O_2$ concentration increases the difference vanishes.

The higher domination of reaction 2 in the membrane reactor, as shown in Fig. 7, as well as the reaction rate differences in Fig. 9, can explain the overall higher C2 selectivity (and consequently yields) compared to the fixed bed reactor as shown in Fig. 5.

Another observation seen in Fig. 5 is the decline in selectivity for both reactors as the temperature increases, this can be understood by looking at the reactions that are generating and consuming $C_2H_4$ in the kinetic model. As shown in Table I, reactions 5 and 7 are generating, while reactions 6 and 8 are consuming $C_2H_4$. The reaction rates of these four reactions were integrated over the domain using Eq. 18, and then consuming reaction contributions are normalized by the total of the generation reactions as shown in Eqs. 20 and 21.

$$\%C_2H_4 \quad Consumption \quad r_6 = \frac{RC_6}{RC_5 + RC_7} \qquad [20]$$

$$\%C_2H_4 \quad Consumption \quad r_8 = \frac{RC_8}{RC_5 + RC_7} \qquad [21]$$

Equations 20 and 21 were evaluated for both reactors at all operating temperatures and the results are plotted in Fig. 10. In Fig. 10a, the consumption of $C_2H_4$ generally increases with temperature, and the overwhelming contribution is coming from reaction 8 as it consumes almost 70% percent of the generated $C_2H_4$ in case of the fixed-bed reactor at 1073 K. The increase in $C_2H_4$ consumption can be understood by plotting the reaction rates for reaction 5, 7, and 8 with constant pressures and only varying temperature. As shown in Fig. 10b, $C_2H_4$ consuming reaction 8 scales more significantly with temperature compared to the reactions

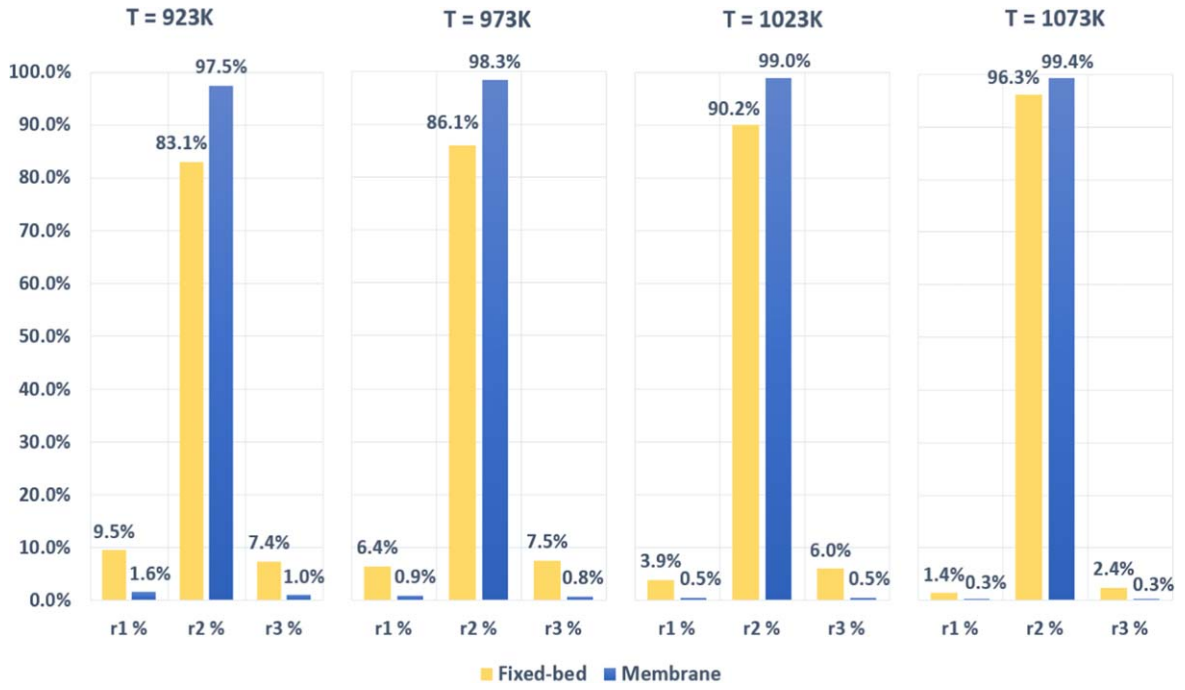


**Figure 7.** Contribution percentage of each reaction in $CH_4$ consumption.

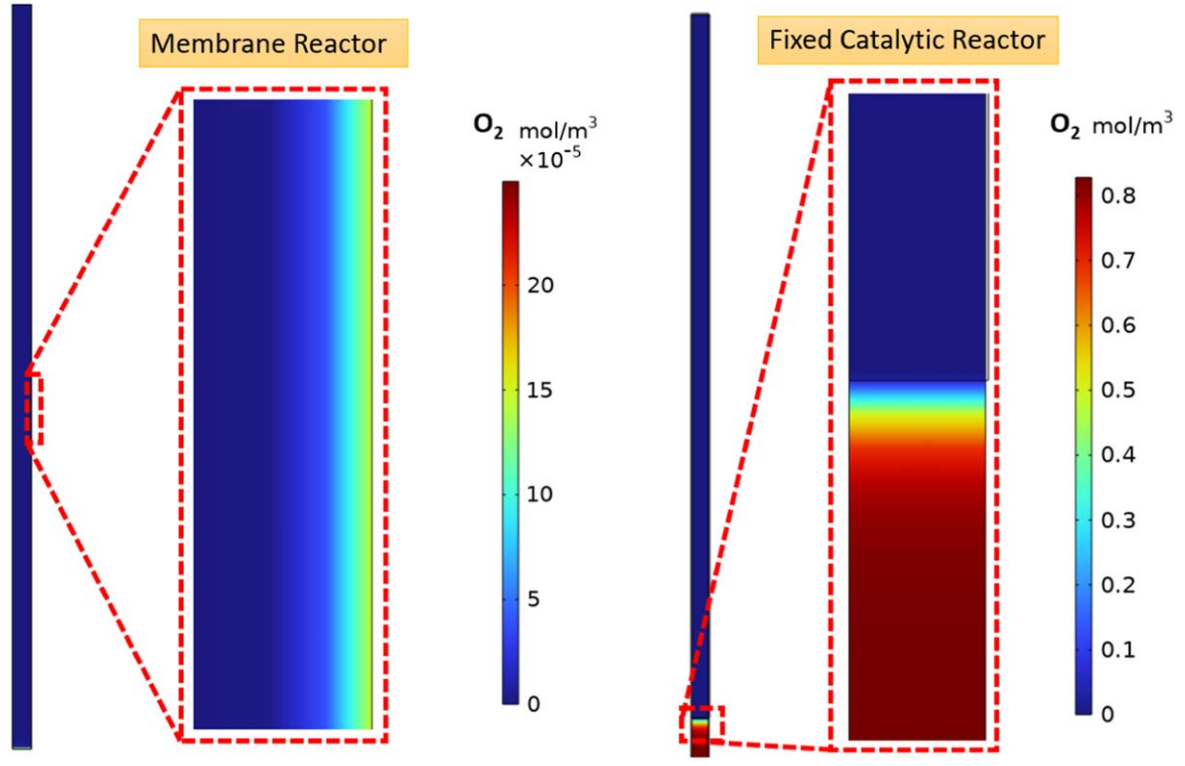


**Figure 8.** Oxygen concentration in the reaction zone for both reactors.

that are generating $C_2H_4$ (reactions 5 and 7), which explains the drop in C2 selectivity that is seen in Fig. 5 for both reactors as temperature increases.

The final part in assessing the performance of the membrane reactor is looking at the potential amount of $H_2$ that can be transported to the feed side, Eqs. 14–16 were used to calculate the gas molar fluxes at the feed side. Although the membrane transports a fairly high number of protons, most of which are converted to $H_2O$ at the feed side because of the gas composition. The values for the gas molar fluxes at the feed side are shown below in Fig. 11.

The $H_2$ gas molar flux can be improved by reducing the $O_2$ fraction on the feed side, but this will reduce the overall oxide ion transfer to the sweep side and will negatively affect the reactor performance. It was shown before using DFT calculation, that molten carbonate can also conduct protons and oxide ions.[18,29–31] So, using a composite membrane of molten carbonate + BZY might

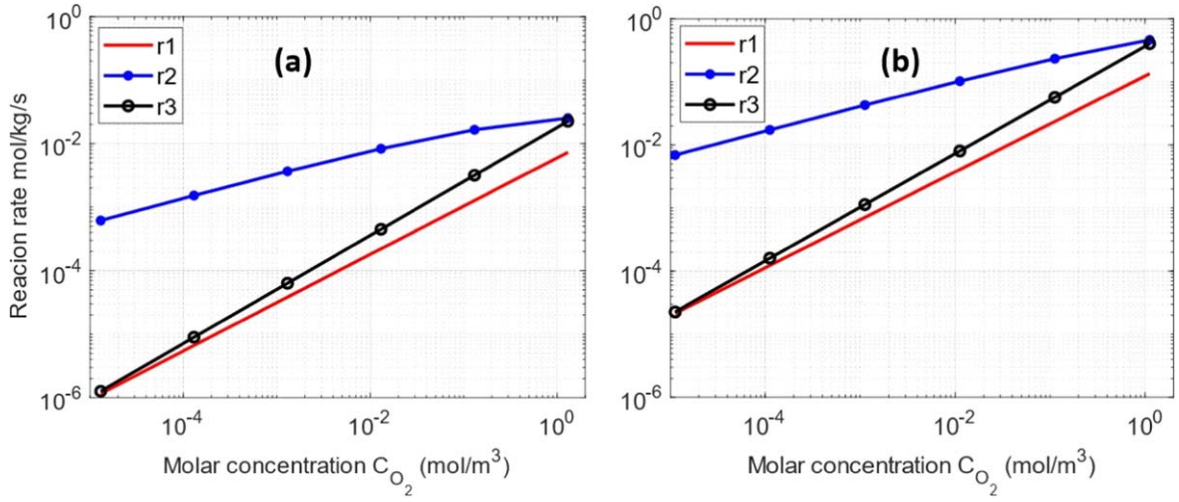


**Figure 9.** Reaction rate for reactions 1, 2, and 3, at (a) T = 923 K and (b) T = 1073 K.

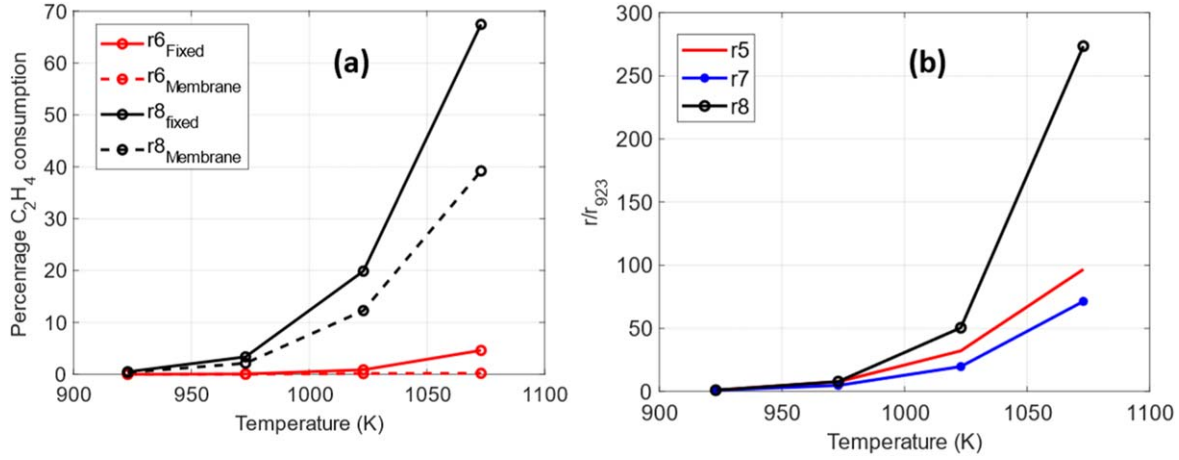


**Figure 10.** (a) Contributions of r6 and r8 in consuming $C_2H_4$ (b) reaction rate (normalized by its value under 923 K) for reaction 5, 7, and 8.

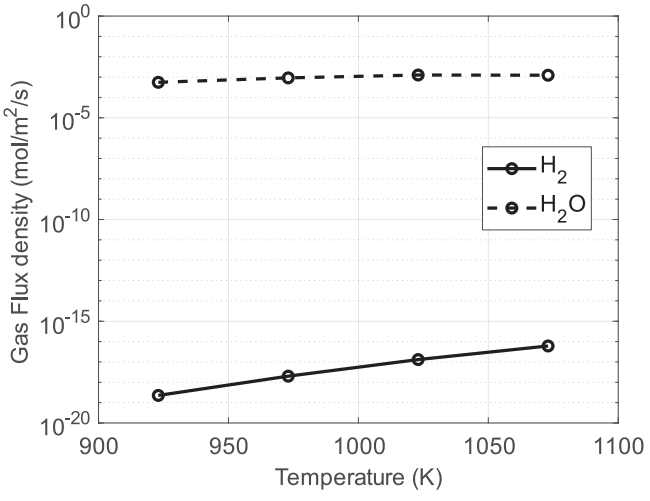


**Figure 11.** Gas molar flux densities at the feed side.

increase the overall conductivity and produce a decent $O_2$ molar flux at the sweep side despite having a low $O_2$ concentration gradient across the membrane.

## Conclusions

In this research, we have developed a numerical model to simulate a new $H_2/O_2$ co-transport membrane (HOTM) reactor for combined $H_2O/H_2$ removal and C2 production. To validate the thermodynamic and transport properties simultaneously of the membrane, we implemented a two-step validation procedure. Firstly, we utilized the experimental data of $OH_O$ ion concentration reported by Kreuer[21] to inversely obtain the thermodynamic properties (Enthalpy and entropy of reactions). Then, we used the conductivities provided by Nomura [17] to calculate the transport properties (pre-exponential factor and activation energy of each charged species). After validation, the model-predicated C2 yield and $CH_4$ conversion rate of the membrane reactor have been compared against the state-of-the-art fixed-bed reactor with the same dimensions and operating conditions. The results indicate that the membrane reactor provides more control on providing $O_2$ uniformly to the catalytic reaction bed compared to the conventional co-fed fixed-bed reactor. In addition, the gradual feeding of $O_2$ along the reactor length led to better efficiency in producing the desired C2 products. Furthermore, the membrane reactor could remove $H_2O$ and $H_2$ from the reactor simultaneously but due to the gas composition at the feed side, most of the transported protons will be converted to water. The model could be used as a guidance tool for experimentalists to design new HOTM reactors and overcome the challenges in achieving high $CH_4$ conversion at high C2 selectivity.

## Acknowledgments

This material is based upon work supported by the U.S. National Science Foundation under grant number CBET-1924095.

## ORCID

Kevin Huang https://orcid.org/0000-0002-1232-4593
Xinfang Jin https://orcid.org/0000-0002-3148-4904

## References

1. A. Cruellas, T. Melchiori, F. Gallucci, and M. V. S. Annaland, "Oxidative coupling of methane: a comparison of different reactor configurations." *Energy Technol.*, **8**, 1900148 (2020).
2. B. L. Farrell, V. O. Igenegbai, and S. Linic, "A viewpoint on direct methane conversion to ethane and ethylene using oxidative coupling on solid catalysts." *ACS Catal.*, **6**, 4340 (2016).
3. M. C. Alvarez-Galvan, N. Mota, M. Ojeda, S. Rojas, R. M. Navarro, and J. L. Fierro, "Direct methane conversion routes to chemicals and fuels." *Catal. Today*, **171**, 15 (2011).
4. A. Cruellas, T. Melchiori, F. Gallucci, and M. V. S. Annaland, "Advanced reactor concepts for oxidative coupling of methane." *Catal. Rev.*, **59**, 234 (2018).
5. G. E. Keller and M. M. Bhasin, "Synthesis of ethylene via oxidative coupling of methane: I. Determination of active catalysts." *J. Catal.*, **73**, 9 (1982).
6. C. A. Gärtner, A. C. V. Veen, and J. A. Lercher, "Oxidative dehydrogenation of ethane: common principlesand mechanistic aspects." *ChemCatChem*, **5**, 3196 (2013).
7. S. J. Han, S. W. Lee, H. W. Kim, S. K. Kim, and Y. T. Kim, "Nonoxidative direct conversion of methane on silica-based iron catalysts: effect of catalytic surface." *ACS Catal.*, **9**, 7984 (2019).
8. Y. Shu, D. Ma, L. Xu, Y. Xu, and X. Bao, "Methane dehydro-aromatization over Mo/MCM-22 catalysts: a highly selective catalyst for the formation of benzene." *Catal. Lett.*, **70**, 67 (2000).
9. N. Yaghobi and M. H. R. Ghoreishy, "Oxidative coupling of methane in a fixed bed reactor over perovskite catalyst: a simulation study using experimental kinetic model." *J. Nat. Gas Chem.*, **17**, 8 (2008).
10. A. L. Tonkovich, R. W. Carr, and R. Aris, "Enhanced $C_2$ yields from methane oxidative coupling by means of a separative chemical reactor." *Science*, **262**, 221 (1993).
11. S. Jašo and H. Arellano-Garcia, "Oxidative coupling of methane in a fluidized bed reactor: influence of feeding policy, hydrodynamics, and reactor geometry." *Chem. Eng. J.*, **171**, 255 (2011).
12. X. Li, K. Huang, N. Van Dam, and X. Jin, "Performance projection of a high-temperature $CO_2$ transport membrane reactor for combined $CO_2$ capture and Methane-to-Ethylene conversion." *J. Electrochem. Soc.*, **169**, 053501 (2022).
13. Y. K. Kao, L. Lei, and Y. S. Lin, "A comparative simulation study on oxidative coupling of methane in fixed-bed and membrane reactors." *Ind. Eng. Chem. Res.*, **36**, 3583 (1997).
14. S. Bhatia, C. Y. Thien, and A. R. Mohamed, "Oxidative coupling of methane (OCM) in a catalytic membrane reactor and comparison of its performance with other catalytic reactors." *Chem. Eng. J.*, **148**, 525 (2009).
15. W. Wang and Y. S. Lin, "Analysis of oxidative coupling of methane in dense oxide membrane reactors." *J. Membr. Sci.*, **103**, 219 (1995).
16. V. V. Thyssen, V. B. Vilela, D. Zanetti de Florio, A. S. Ferlauto, and F. C. Fonseca, "Direct conversion of methane to $C_2$ hydrocarbons in solid-state membrane reactors at high temperatures." *Chem. Rev.*, **122**, 3966 (2021).
17. K. Nomura and H. Kageyama, "Transport properties of $Ba(Zr_{0.8}Y_{0.2})O_{3-\delta}$ perovskite." *Solid State Ion.*, **178**, 661 (2007).
18. X. Lei, K. Huang, and C. Qin, "Proton transfer in molten lithium carbonate: mechanism and kinetics by density functional theory calculations." *Sci. Rep.*, **7**, 7381 (2017).
19. K. Liu, F. Meng, D. Zhu, Z. Wang, S. Lou, J. Zhao, H. Xiao, and Y. Tang, "Conversion of methane facilitated by solid oxide electrolysis cells." *Chem. Eng. Technol.*, **43**, 2007 (2020).
20. S. H. Morejudo et al., "Direct conversion of methane to aromatics in a catalytic co-ionic membrane reactor." *Science*, **353**, 563 (2016).
21. K. D. Kreuer, S. Adams, W. Münch, A. Fuchs, U. Klock, and J. Maier, "Proton conducting alkaline Earth zirconates and titanates for high drain electrochemical applications." *Solid State Ion.*, **145**, 295 (2001).
22. R. P. O'Hayre, M. D. Sanders, E. Vøllestad, B. W. Hildenbrand, H. Zhu, and R. J. Kee, "Modeling the steady-state and transient response of polarized and non-polarized proton-conducting doped-perovskite membranes." *J. Electrochem. Soc.*, **160**, F290 (2013).
23. Z. Stansch, L. Mleczko, and M. Baerns, "Comprehensive kinetics of oxidative coupling of methane over the $La_2O_3$/CaO catalyst." *Ind. Eng. Chem. Res.*, **36**, 2568 (1997).
24. C. T. Tye, A.-R. Mohamed, and S. Bhatia, "Modeling of catalytic reactor for oxidative coupling of methane using $La_2O_3$/CaO catalyst." *Chem. Eng. J.*, **87**, 49 (2002).
25. T. He, K. D. Kreuer, Y. M. Baikov, and J. Maier, "Impedance spectroscopic study of thermodynamics and kinetics of a Gd-doped $BaCeO_3$ single crystal." *Solid State Ion.*, **95**, 301 (1997).
26. W. Wang and A. V. Virkar, "Ionic and electron–hole conduction in $BaZr_{0.93}Y_{0.07}O_{3-\delta}$ by 4-probe dc measurements." *J. Power Sources*, **142**, 1 (2005).
27. S. Ricote, N. Bonanos, and G. Caboche, "Water vapour solubility and conductivity study of the proton conductor $BaCe_{(0.9-x)}Zr_xY_{0.1}O_{(3-\delta)}$." *Solid State Ion.*, **180**, 990 (2009).
28. S. Choi, C. J. Kucharczyk, Y. Liang, X. Zhang, I. Takeuchi, H.-I. Ji, and S. M. Haile1, "Exceptional power density and stability at intermediate temperatures in protonic ceramic fuel cells." *Nat. Energy*, **3**, 202 (2018).
29. X. Lei, K. Huang, and C. Qin, "Enhanced interfacial proton migration on $BaZr(Y)O_3$ by molten carbonate: a first principles study." *Solid State Ion.*, **289**, 48 (2016).
30. X. Lei, K. Haines, K. Huang, and C. Qin, "Density functional theory study of oxygen migration in molten carbonate." *J. Power Sources*, **305**, 161 (2016).
31. X. Lei, C. Qin, and K. Huang, "Energetics of proton transfer in alkali carbonates: a first principles calculation." *RSC Adv.*, **5**, 56205 (2015).
32. ToolBox, E, (2018), [Online]. Available: Air - diffusion coefficients of gases in excess of air https://engineeringtoolbox.com/air-diffusion-coefficient-gas-mixture-temperature-d_2010.html [Accessed 8 2022].